The Kinematics and Morphologies of Coronal Mass Ejections using Multiscale Methods

by

Jason P. Byrne, B.A.(Mod.), Dip. Stat.

Astrophysics Research Group

Supervisor: Dr. Peter T. Gallagher



Abstract

The magnetic field of the Sun is embedded in the plasma and undergoes large twisting and shearing as stresses build up through differential rotation. Sometimes the strain is released in an explosive manner such as a flare or coronal mass ejection (CME) whereby twisted fields restructure themselves into lower energy configurations. The explosive nature of these phenomena is attributed to magnetic reconnection. Numerous models of the magnetic field have been devised to explain how a CME is initiated and propagates into the solar corona and interplanetary space since they were first observed by the Solar Maximum Mission over 30 years ago.

The diffuse morphology and transient nature of CMEs makes them difficult to identify and track using traditional image processing techniques. Previous CME studies have been limited to running- or fixed-difference techniques where the subtraction of subsequent images increases the intensity of moving features but also increases the errors involved. Other methods which involve a user performing point-and-click measurements increases errors due to the subjective nature of the work. We apply multiscale image processing methods to enhance the visibility of the faint CME front in single images. This enables an ellipse characterisation to objectively study the changing morphology and kinematics of a sample of events imaged by the Large Angle Spectrometric Coronagraph (LASCO) onboard the Solar and Heliospheric Observatory (SOHO) and the Sun Earth Connection Coronal and Heliospheric Investigation (SECCHI) onboard the Solar Terrestrial Relations Observatory (STEREO). The high accuracy of these methods allows us to test the CMEs for non-constant acceleration and expansion, and non-linear propagation through the solar corona.

The kinematic evolution of some of the CMEs studied with our methods have been shown to differ from existing catalogues. These catalogues are based upon running-difference techniques which can lead to over-estimating CME heights and widths. Our resulting kinematic curves are not well fitted with the constant acceleration model, which has long been the standard approximation and is also predicted by the well known "breakout model" of CME theory. We found that some events have high acceleration below ~5 solar radii, indicative of an acceleration regime in low corona fields-of-view. Furthermore, we find that the CME angular widths measured by these catalogues are over-estimated, and indeed for some events our analysis shows non-constant CME expansion across the plane-of-sky.

These methods have been designed with future automation in mind. This would enable a full statistical study of numerous CMEs observed by SOHO during its lifetime and indeed be of use for future STEREO data and for the upcoming Solar Dynamics Observatory (SDO) mission. A large kinematic and morphological study will be of great benefit in testing current theoret-

ical models. The combined view-points of the STEREO spacecraft will also be of benefit in obtaining the true CME kinematics and morphology through a triangulation in 3D space.

Contents

Al	strac	et e e e e e e e e e e e e e e e e e e	i		
1	Intr	oduction	1		
	1.1	The Solar Atmosphere	1		
	1.2	Coronal Mass Ejections	3		
	1.3	Image Processing of CMEs	6		
2	Inst	rumentation & Data	8		
	2.1	SOHO/LASCO	8		
	2.2	STEREO/SECCHI	9		
3	Data	a Analysis	11		
	3.1	Multiscale Filtering	12		
	3.2	Characterising the CME Front	14		
	3.3	Error Analysis & Model Fitting	15		
4	Resu	ults	17		
	4.1	Slow CME: 2004 April 1	17		
	4.2	Fast CME: 2002 April 21	18		
	4.3	Summary	20		
5	Forward Plan				
	5.1	Automation	22		
	5.2	STEREO Twin Views	22		
	5.3	Error Analysis	22		
	5.4	Model Comparisons	23		
	5.5	Multiscale tool development	23		

Contents	IV
6 List of Publications & Presentations	25
Bibliography	27

Chapter 1

Introduction

"NASA's Living With a Star program is predicated on the fact that CMEs are the most important aspect of solar activity affecting the Earth and interplanetary space."

- Dr. Brian Dennis, NASA/GSFC, 2005

Coronal mass ejections (CMEs) are large-scale eruptions of plasma and magnetic field with energies up to, and beyond, 10^{32} ergs. The mass of particles expelled in a CME can amount to 10^{15} g, typically traveling from the Sun at velocities of hundreds up to several thousand kilometers per second [11, 14, 10, 9]. They can lead to significant geomagnetic disturbances on Earth, visible as aurorae, and may have negative impacts upon space-borne instruments susceptible to high levels of radiation when outside the protection of Earth's magnetosphere. While they have been investigated by remote sensing and in situ measurements for more than 30 years, their kinematic and morphological evolution through the corona and interplanetary space is still not completely understood. In this report we outline methods used to examine the kinematics and morphologies of CMEs as they travel through the solar corona. This involves data acquisition and preprocessing, advanced image processing, and CME characterisation. Subsequent error analysis allows a comparison with the predictions of theoretical models.

1.1 The Solar Atmosphere

A stellar atmosphere is composed of all outer regions lying above the core, radiative and convective zones. It can be separated into distinct regimes dependent on the density and temperature profiles. This is plotted for the Sun in Fig. 1.1 and the regions are split up into photosphere, chromosphere, transition region, and corona.

The surface of the Sun is the photosphere which has an average temperature of 5800 K, a density of 10^{23} m⁻³ and a depth of less than 500 km. Cooler regions called sunspots have temperatures of 4000–4500 K and are due to intense magnetic field activity. Granulation of the photosphere occurs when hot plasma rises to the surface, and outer granule edges appear darker due to cooler descending plasma. Granules range in diameter from 150–2500 km.

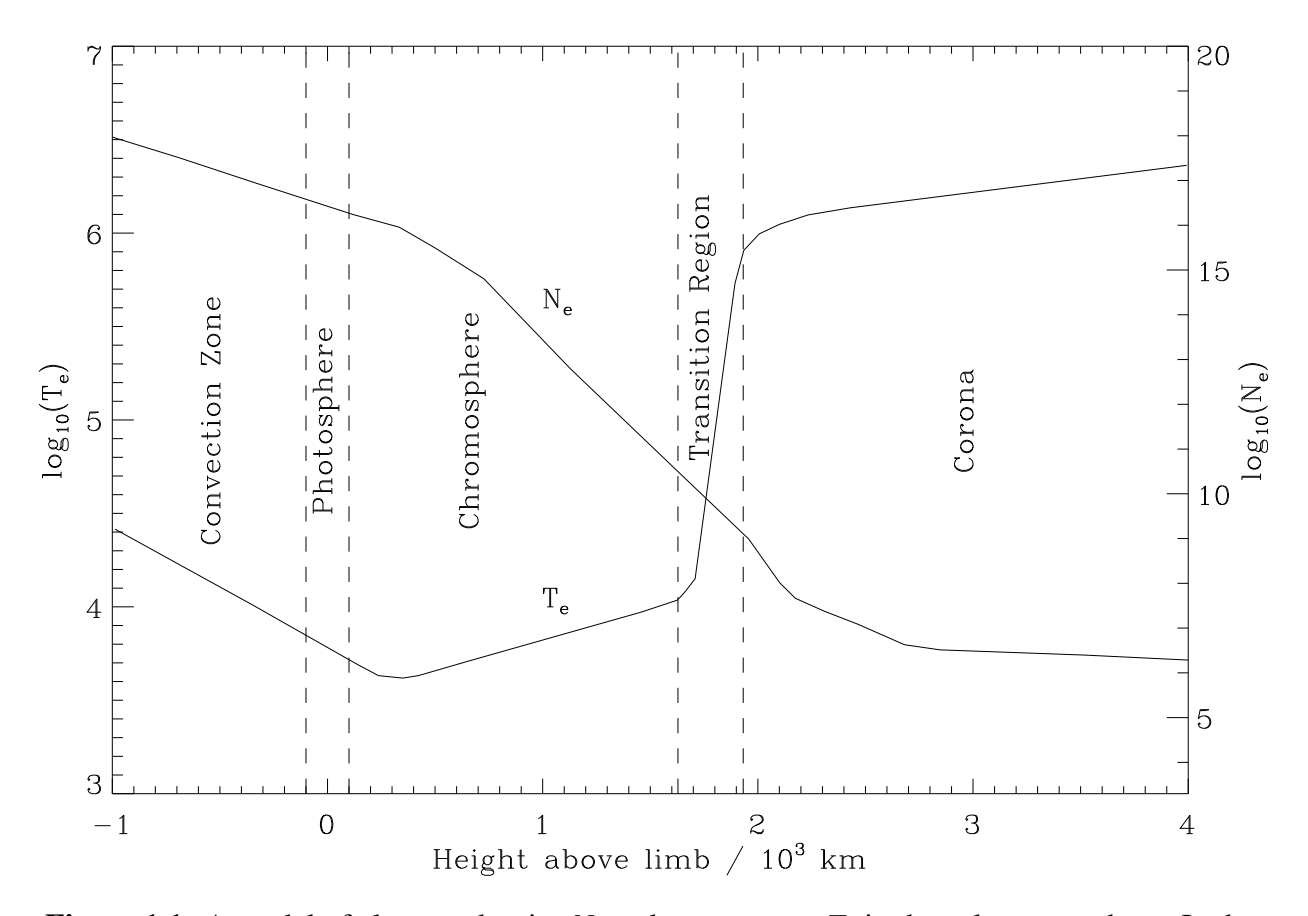


Figure 1.1: A model of electron density N_e and temperature T_e in the solar atmosphere. In the chromosphere, the plasma is only partially ionized. The plasma becomes fully ionized at the sharp transition from chromospheric to coronal temperatures. (Gallagher, 1999).

Above the photosphere lies the chromosphere where the temperature ranges from 4500–20000 K. The density falls by a factor of almost a million from bottom to top, so the magnetic field dominates the chromospheric structure. The most prominent structure seen on the limb are columns of plasma called spicules which can typically reach 3000–10000 kilometres above the Sun's surface and are very short-lived (rising and falling over 5~10 minutes).

Between the chromosphere and corona lies the transition region where the temperature jumps rapidly to nearly one million kelvin. It is only about 100 km thick and it marks the point where magnetic forces dominate completely over gravity, gas pressure and fluid motion.

The outermost part of the solar atmosphere is the corona, extending millions of kilometres into space. It is 10^{-12} times as dense as the photosphere so it produces about 10^{-6} times as much visible light. It is seen in white light with the use of a coronagraph which blocks out the solar disc to enhance the visibility of the coronal emission. It composes three parts: the K-corona scattering of sunlight by free electrons, the F-corona scattering of sunlight by interplanetary dust particles, and the E-corona emission from highly ionized atoms such as Fe X. The temperature of the corona is in the region of 2 MK or hotter across regions of increased magnetic field density (such as above active regions/sunspots), or cooler across regions of open field lines (coronal holes).

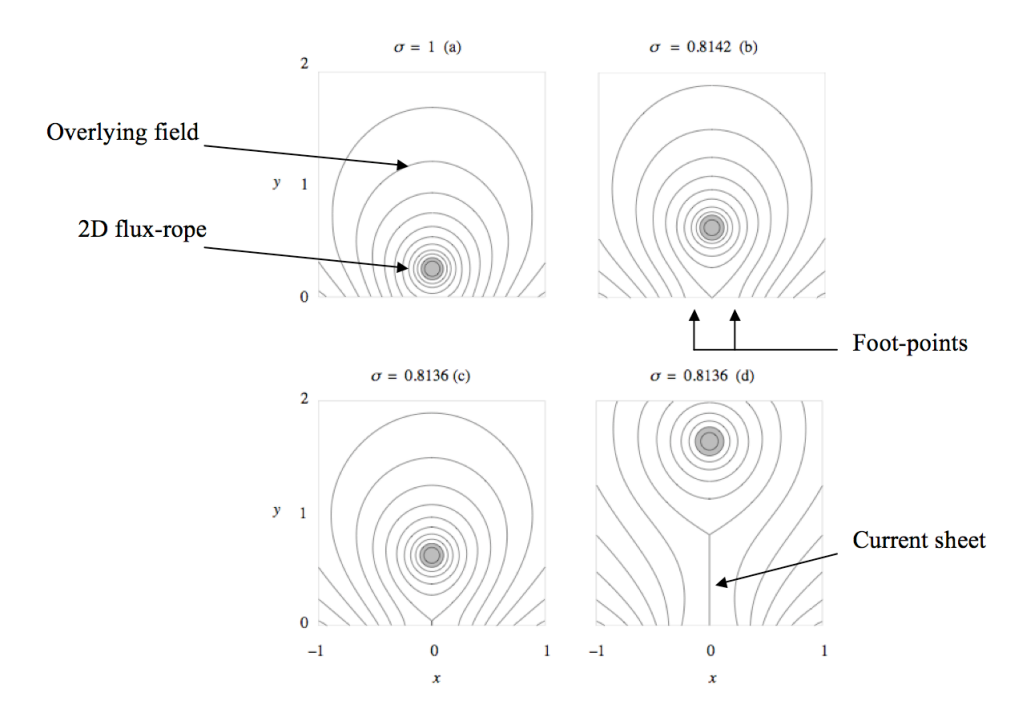


Figure 1.2: Theoretical height-time evolution of a 2D flux-rope. The flux-rope rises slowly from a to b to c as the foot-point separation σ is decreased, and then jumps abruptly from c to d.

The solar wind is the constant out stream of charged particles of plasma ejected from the Sun's atmosphere due to the kinetic energy imparted to them at such high temperatures. It consists mostly of electrons and protons at energies of ~ 1 KeV, traveling at speeds of 400 km/s (slow solar wind) up to 800 km/s (fast solar wind, found in regions of open field lines such as coronal holes).

1.2 Coronal Mass Ejections

"We define a coronal mass ejection (CME) to be an observable change in coronal structure that 1) occurs on a time scale of a few minutes and several hours and 2) involves the appearance (and outward motion) of a new, discrete, bright, white light feature in the coronagraph field of view."

- Hundhausen et al., 1984

CMEs are the largest manifestation of the shedding of solar magnetic field during the Sun's 22 year cycle. Every 11 years the magnetic axis of the Sun flips, giving rise to periodic patterns in the activity called solar minimum and maximum. At solar minimum a CME may occur up to once a week but during solar maximum they can be as frequent as three a day. In cases of halo CMEs coming toward the Earth, the higher particles densities and energies involved can

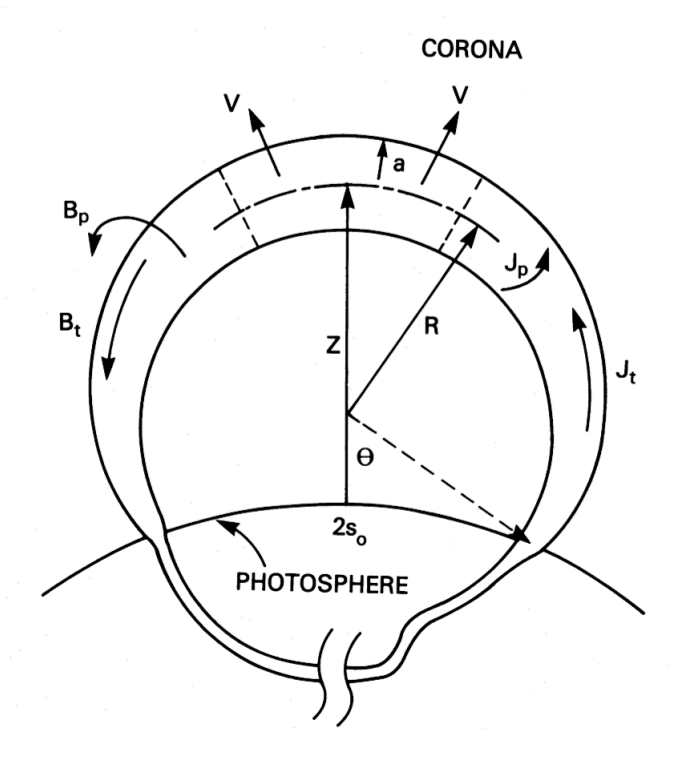


Figure 1.3: A schematic of the proposed 3D flux-rope model. Components of the current density **J** and magnetic field **B** are shown, where subscripts "t" and "p" refer to the toroidal and poloidal directions respectively. The radius of curvature is R, the apex height is Z and the footpoint separation is $2s_0$.

cause geomagnetic storms, especially if the magnetic orientation of the CME is oppositely directed to that of Earth's magnetosphere. This is referred to as space weather, and understanding this interaction is of considerable practical importance because technological systems, such as communications and navigation satellites, can suffer interruptions or damage. To this end, missions such as SOHO and the recent STEREO have been launched to study the initiation and propagation of CMEs through the solar corona and interplanetary space.

It is well known that CMEs are associated with filament eruptions and solar flares [30, 20] but the driver mechanism remains elusive. Several theoretical models have been developed in order to describe the forces responsible for CME initiation and propagation. Within the context of magnetohydrodynamics, we can describe the solar plasma as a fluid with the assumption that there is negligible viscosity, so the equation of motion becomes:

$$\rho \frac{D\mathbf{v}}{Dt} = \mathbf{j} \times \mathbf{B} - \nabla P + \rho \mathbf{g} - \rho A_{cme} C_D \mathbf{v}^2$$
(1.1)

with density ρ , pressure P, velocity \mathbf{v} , current density \mathbf{j} , magnetic field \mathbf{B} , and gravity \mathbf{g} . The CME drag force also considers the cross-sectional area A_{cme} and drag coefficient C_D [4]. The Lorentz force $\mathbf{j} \times \mathbf{B}$ is thought to be the dominant driver force in modeling CME eruptions.

In the two-dimensional flux-rope model [24, 15, 8] the CME is assumed to be initially located at the centre of a bi-polar field configuration as shown in Fig. 1.2a. The field foot-point separation

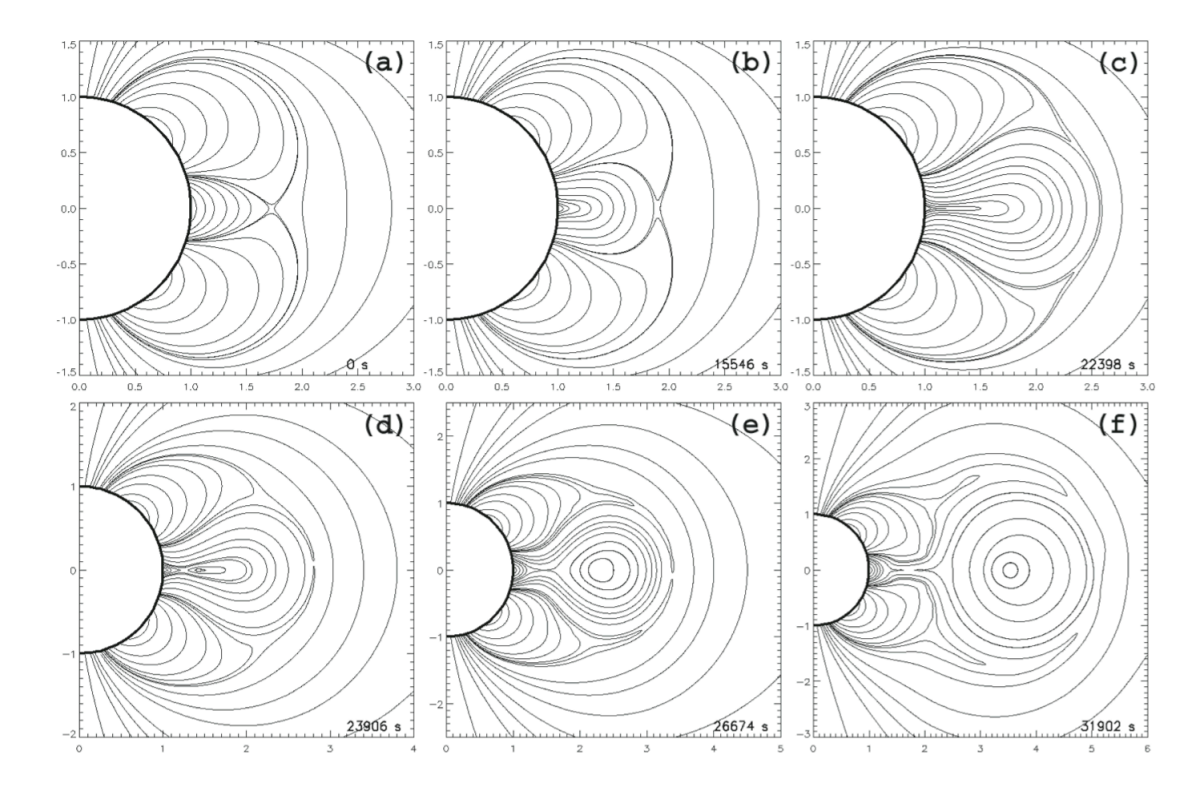


Figure 1.4: Schematic of the breakout model showing a meridional projection of the magnetic field lines throughout the process. The axes units are R_{\odot} , and the elapsed simulation time is indicated at the bottom right of each panel [18].

 (σ) is gradually decreased, and an eruption is triggered by a loss of equilibrium or instability in the field. The flux-rope then accelerates away from the surface as overlying fields are sequentially disconnected from the surface by magnetic reconnection (Fig. 1.2b-d).

A more recent model that builds on this, is the three-dimensional magnetic flux-rope model illustrated in Fig. 1.3 [16, 6]. This model assumes that the kinematics of an erupting flux-rope can be described using the force-balance equation (1.1), where the motion in the low corona is dominated by the radial force, neglecting the effects of gravity and drag. Essentially the structure of the flux-rope introduces a hoop force due to the toroidal current component within. The eruption is initiated by the injection of poloidal flux, and the subsequent acceleration can be expressed as

$$\frac{d\mathbf{v}}{dt} \sim \frac{\Phi_p^2}{[R \ln(8R/a_f)]^2} f_R \tag{1.2}$$

where Φ_p is the poloidal magnetic flux inside the flux-rope, f_R the radial force, a_f the flux-rope radius, and R its radius of curvature (see [6] for details). The flux-rope acceleration is therefore dependent on its geometrical properties, including its width and radius.

An alternative to these flux-rope models is the magnetic break-out model in which the CME eruption is triggered by reconnection between the overlying field and a neighbouring flux system, illustrated in Fig. 1.4 ([1, 18, 19]). It starts by shearing a potential field configuration,

which adds magnetic pressure to the inner flux system and causes it to expand and distort the overlying field, eventually forming a thin current sheet.. As the current sheet grows, reconnection begins, thereby creating a passage for the CME release. A current sheet also forms beneath the erupting sheared field, creating a disconnected flux-rope that escapes. The increased rate of outward expansion drives a faster rate of breakout reconnection yielding the positive feedback required for an explosive eruption.

The models are dependent on geometrical properties of the CME, and they are designed to give an indication of the processes that drive CME kinematics. Thus it is important to develop methods of localising the CME front and characterising it in the observed data with high accuracy for model comparisons.

1.3 Image Processing of CMEs

Current methods of CME detection have their limitations, mostly since these diffuse objects have been difficult to identify using traditional image processing techniques. These difficulties arise from the transient nature of the CMEs, the scattering effects and non-linear intensity profile of the surrounding corona, and the interference of cosmic rays and solar energetic particles (SEPs) appearing as noise on the coronagraph detectors. Observations made SOHO/LASCO are compiled into a CME catalog at the Coordinated Data Analysis Workshop (CDAW, [28]) which operates by tracking the CME in C2 and C3 running difference images to produce height-time plots of each event. It is a wholly manual procedure and is subject to user bias in interpreting the data. The Computer Aided CME Tracking routine (CACTus, [25]) is also based upon C2 and C3 running difference images. The images are unwrapped into polar coordinates and angular slices are stacked together in a time-height plot. CMEs thus appear as ridges in these plots, detected by a Hough Transform. The nature of this detection constrains the CMEs to have constant velocity and zero acceleration. The Solar Eruptive Event Detection Systems (SEEDS, [22]) is an automatic detection based on C2 running difference images only, unwrapped into polar coordinates. The algorithm uses a form of threshold segmentation to approximate the shape of the CME leading edge, and automatically determines the height, velocity and acceleration profiles from it.

In this work we apply a new multiscale method of analysing CMEs. The use of multiscale methods in astrophysics have proven effective at denoising spectra and images [21, 7], analysing solar active region evolution [12], and enhancing solar coronal images [26, 27]. A particular application of multiscale decompositions uses high and low pass filters convolved with the image data to exploit the multiscale nature of the CME [29]. This highlights its intensity against the background corona as it propagates through the field-of-view, while neglecting small scale features (essentially denoising the data). It also leads to the use of nonmaxima suppression to trace the edges in the CME images. With these methods for defining the front of the CME we

can characterise its morphology (width, orientation) and kinematics (position, velocity, acceleration) in coronagraph images. Multiscale analysis also has the benefit of working on independent images without any need for differencing, so the temporal errors involved are on the order of the exposure time of the instrument (~ a few seconds).

Chapter 2

Instrumentation & Data

2.1 SOHO/LASCO

SOHO is a joint European Space Agency (ESA) and National Aeronautics and Space Administration (NASA) mission, launched on December 2, 1995. Situated in orbit about the first Lagrangian or L1 point (where the gravational pull of the earth is cancelled out by that of the Sun) some 1.5 million kilometers from Earth, the SOHO satellite has an uninterrupted view of the sun.

The LASCO instrument [2] is a set of three coronagraphs C1, C2 and C3 that image the solar corona from 1.1--3, 1.5--6 and 3.7--30 R $_{\odot}$ respectively. The C1 coronagraph has not been in operation since 1998 when contact with the SOHO spacecraft was lost for several weeks. A coronagraph is a device which blocks light from the centre of the telescope to increase the relative intensity of the surrounding light. It was invented by the French astronomer Bernard Lyot in 1939 and it enables us to view the solar corona by removing all light from the solar disk, which is on the order of one million times brighter.

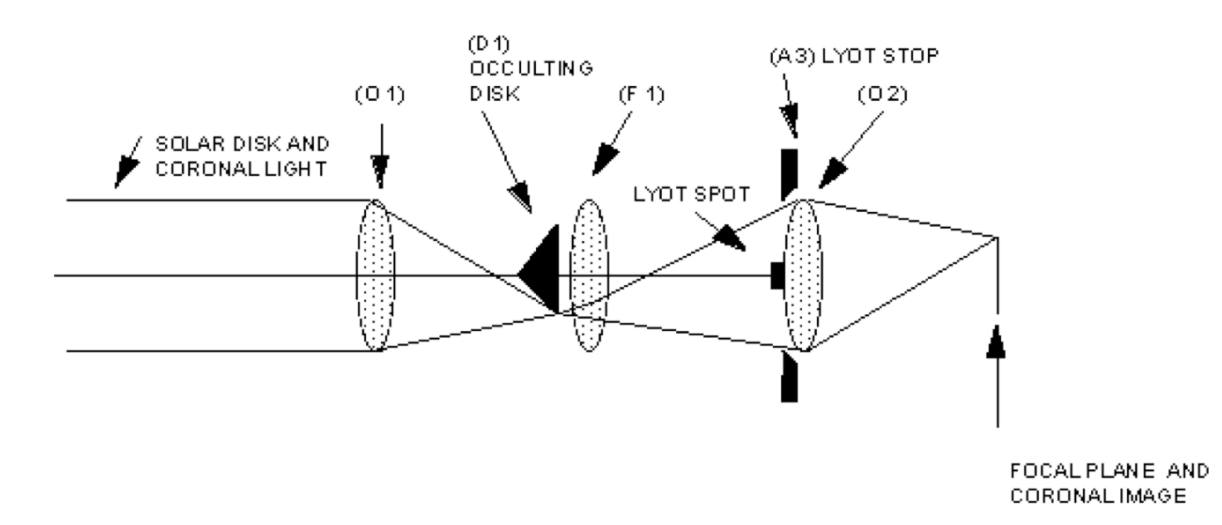


Figure 2.1: A diagram of the internally occulted Lyot coronagraph. The light is incident at objective lens O1, passes occulting disk D1 onto focus lens F1, through to objective lens O2 which has a Lyot stop and spot to prevent stray light occurring on the focal plane image.

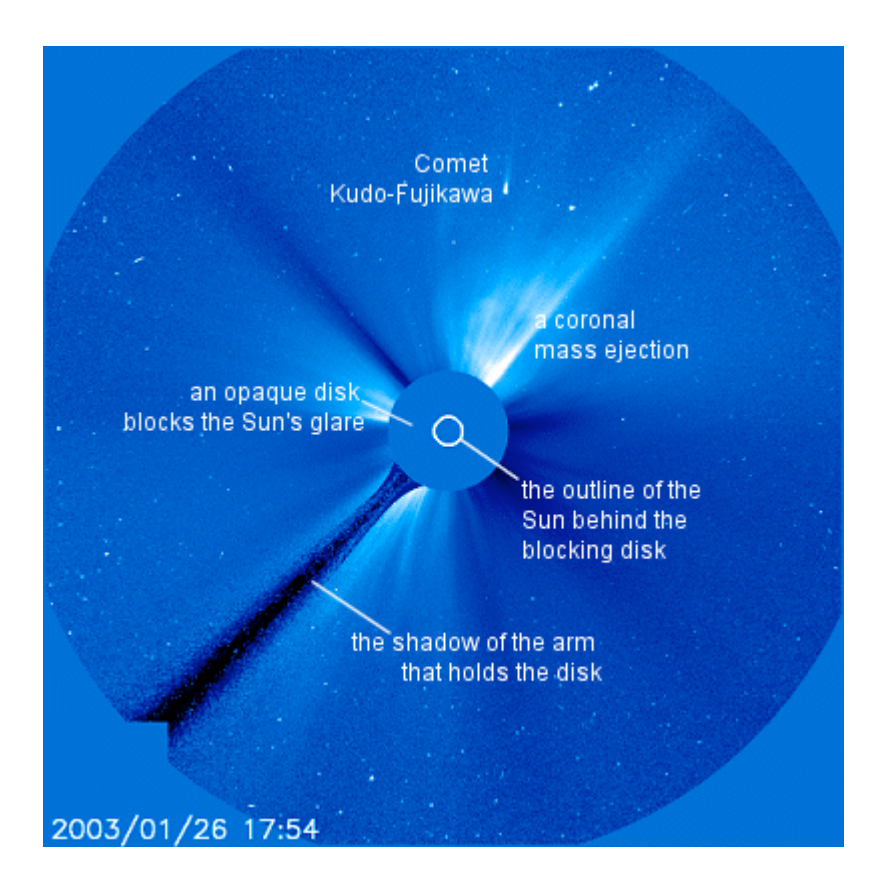


Figure 2.2: A LASCO/C3 coronagraph image showing a faint CME, the occulting disc and arm, and the location of the Sun.

2.2 STEREO/SECCHI

STEREO is the third mission in NASA's Solar Terrestrial Probes program. It employs two nearly identical space-based observatories; one ahead of Earth in its orbit, and the other trailing behind. This arrangement provides the first ever stereoscopic observations of the Sun and solar phenomena, such as CMEs. It was launched on October 25th, 2006 and following a lunar fly-by in December the spacecraft were slingshot into their different orbits. The angular separation of the spacecraft increases by 22 degrees each year, giving the mission a minimum expected lifetime of 2 years. Fig. 2.3 below, illustrates one of the STEREO spacecraft and indicates the positioning of the 4 different instrument suites onboard: SECCHI; In-situ Measurements of Particles and CME Transients (IMPACT); Plasma and SupraThermal Ion Composition (PLASTIC); STEREO/WAVES radio burst tracker (SWAVES).

The SECCHI [13] suite comprises 5 scientific telescopes: firstly the Sun Centred Imaging Package (SCIP) consisting of an Extreme Ultraviolet Imager (EUVI) and 2 coronagraphs (COR1/2) with fields-of-view 1.4–4 and 2–15 R_{\odot} ; and secondly the Heliospheric Imagers (HI) consisting of 2 wide angle visible light imagers positioned on the sides of the STEREO spacecraft for fields-of-view extending out to Earth at 1 A.U.

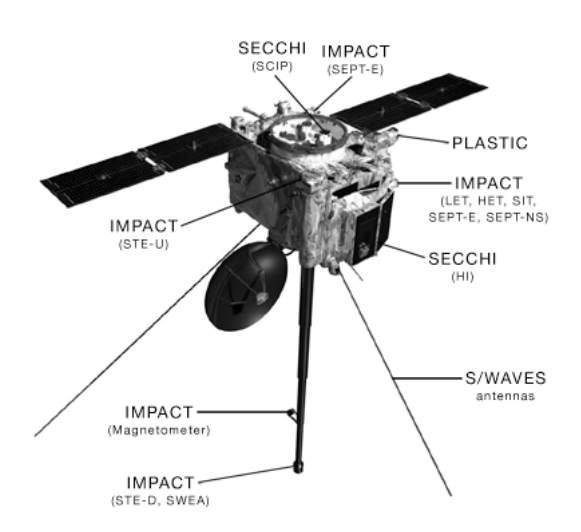


Figure 2.3: Payload diagram of one of the STEREO spacecraft (courtesy of STEREO NASA).

Chapter 3

Data Analysis

The image quality of the coronagraph observations can be diminished for many reasons, including instrumental effects (e.g. scattered light), noise from cosmic rays and SEPs, or data dropouts. We use the following standard preprocessing methods. Firstly the images are normalized with regard to exposure times in order to correct for temporal variations in the image statistics. Secondly a median filter is applied to remove pixel noise, replacing hot pixels with a median value of the surrounding pixel intensities. Finally we perform a background subtraction, obtained from the minimum of the daily median pixels across a time span of a month, and remove the occulting disc with a zero mask. These steps lead to a clear improvement in the image quality for CME study (Fig. 3.1), after which we apply our methods of multiscale analysis.

In recent years the use of wavelets has been increasingly evident in image processing of solar structures [26, 27, 29]. Here we discuss our methods of using multiscale analysis to define the CME front for characterisation.

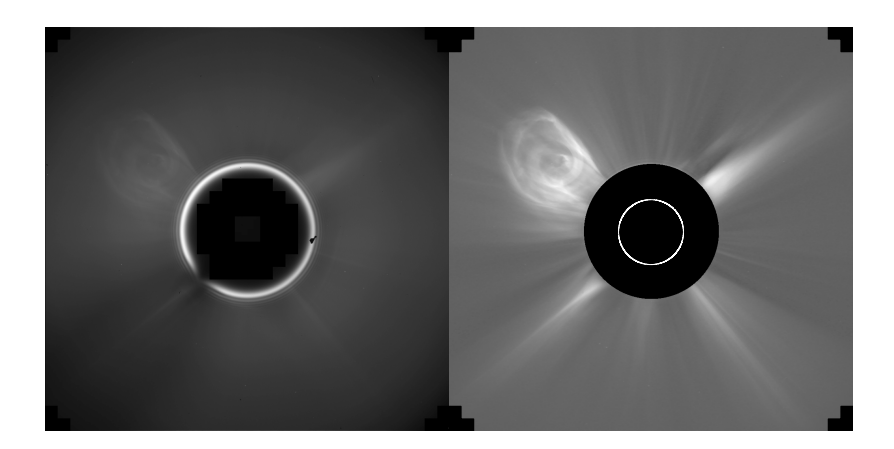


Figure 3.1: Raw (left) and pre-processed image (right) of a CME observed by LASCO on 2004 April 1. The pre-processing includes median filtering, background subtraction and occulter removal.

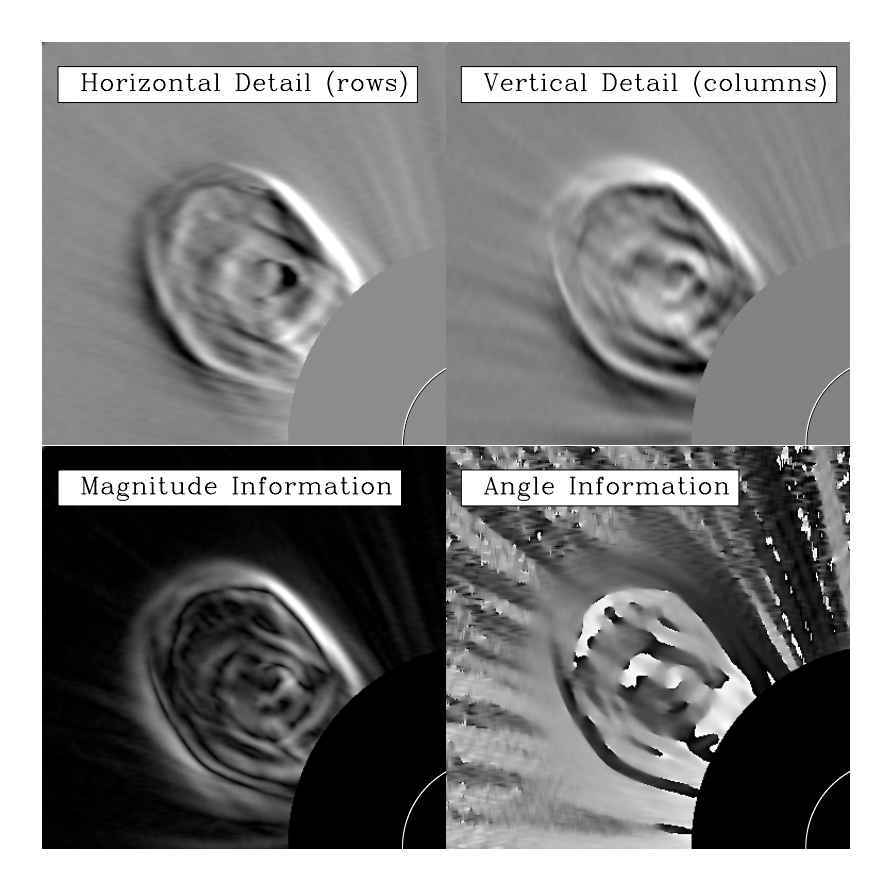


Figure 3.2: Top left, the horizontal, and top right, the vertical coefficients from the high-pass filtering at scale 3. Bottom left, the corresponding magnitude (edge strength) and bottom right, the angle information $(0 - 360^{\circ})$ taken from the gradient space, for a CME observed in LASCO/C2 on 2004 April 1.

3.1 Multiscale Filtering

The fundamental idea behind wavelet analysis is to highlight details apparent on different scales within the data. An example of this is the removal of noise from images, which occurs on small scales only. Wavelets have benefits over previous methods (e.g. Fourier transforms) because they are localised in space and are easily dilated and translated in order to operate on multiple scales, the basic equation being:

$$\psi_{a,b}(t) = \frac{1}{\sqrt{b}}\psi(\frac{t-a}{b}) \tag{3.1}$$

where a and b represent the shifting (translation) and scaling (dilation) of the mother wavelet ψ which can take several forms depending on the required use.

We explore a method of multiscale decomposition in 2D through the use of low and high pass filters; using a discrete approximation of a Gaussian θ and its derivative ψ respectively [26].

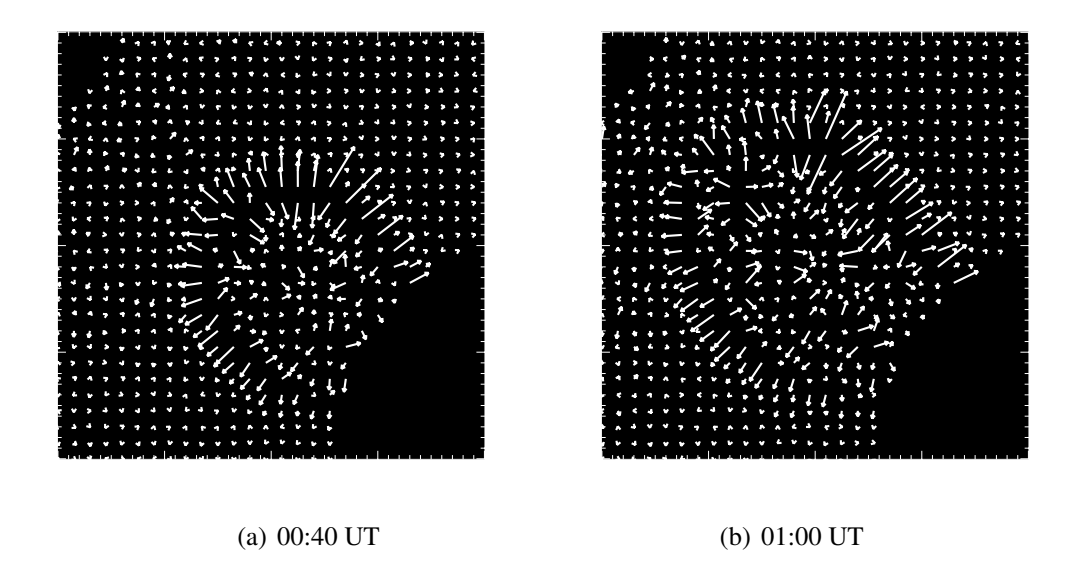


Figure 3.3: The vectors plotted represent the magnitude and angle determined from the gradient space of the high-pass filtering at scale 3. The CME of 2004 April 1 shown here is highlighted very effectively by this method.

Since $\theta(x, y)$ is separable we can write:

$$\psi_x(x,y) = \frac{\partial \theta(x)}{\partial x} \theta(y) \tag{3.2}$$

$$\psi_{y}(x,y) = \theta(x) \frac{\partial \theta(y)}{\partial y}$$
 (3.3)

Successive convolutions of an image with the filters produces the scales of decomposition, with the high-pass filtering providing the wavelet transform of image I(x, y) in each direction:

$$W_x I = W_x I(x, y) = \psi_x(x, y) * I(x, y)$$
 (3.4)

$$W_{y}I = W_{y}I(x,y) = \psi_{y}(x,y) * I(x,y)$$
(3.5)

Akin to a Canny edge detector [29], these horizontal and vertical wavelet coefficients are combined to form the gradient space Γ for each scale:

$$\Gamma(x,y) = \left[W_x I, W_y I\right] \tag{3.6}$$

The gradient information has an angular component α and a magnitude (edge strength) M:

$$\alpha(x,y) = \tan^{-1}\left(W_y I / W_x I\right) \tag{3.7}$$

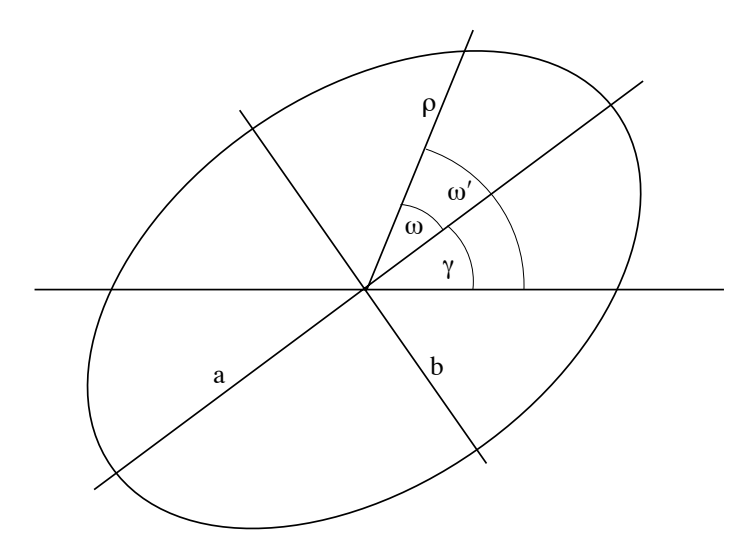


Figure 3.4: Ellipse inclined at angle γ , with semimajor axis a, semiminor axis b, and radial line ρ inclined at angle ω to the semimajor axis.

$$M(x,y) = \sqrt{(W_x I)^2 + (W_y I)^2}$$
 (3.8)

The resultant horizontal and vertical detail coefficients, and the magnitude and angular information are illustrated in Fig. 3.2.

The magnitude information was found to have the highest signal-to-noise ratio at the third scale of the decomposition. This scale is very effective at smoothing unwanted artefacts such as cosmic rays which the median filter may have missed. The angular component α of the gradient specifies a direction which points across the greatest intensity change in the data (an edge). A threshold is specified with regard to this gradient direction in order to chain pixels along maxima, highlighting the edges in the image. We have devised a method of utilising the angular information in a spatiotemporal filter. Overlaying a mesh of vector arrows on the data shows how the magnitude and angular information illustrate the progression of the CME. Each vector is rooted on a pixel in the gradient space, and has a length corresponding to the magnitude M with an angle from the normal α (Fig. 3.3). Using this information, it becomes possible to threshold out the CME with a view to characterising its progression through space. This works by creating a specific detection mask which is used to pull out the edges along the CME front.

3.2 Characterising the CME Front

We introduce using a model such as an ellipse to characterise the CME front across a sequence of images, which has the benefit of providing the kinematics and morphology of a moving and/or expanding structure. The ellipse's multiple parameters, namely its changeable axes lengths and tilts, is adequate for approximating the varying curved structures of CMEs. Chen

et al. [5] suggest an ellipse to be the two-dimensional projection of a flux rope, and Krall and St. Cyr [17] use ellipses to parameterise CMEs and explore their geometrical properties. We fit ellipses to the points determined to be along the CME front by considering a radial fan from Sun centre across the defined edges. This means there are more points along the front than on the flanks of the CME for inclusion in the fit, and the edges never double back on themselves in cases where the CME's internal structure might be otherwise included.

The implementation of the ellipse fitting routine is based upon an initial guess of ellipse centre as the average of the points specified along the front. The ellipse equation (in polar coordinates) is defined as:

$$\frac{\rho^2 \cos^2 \omega}{a^2} + \frac{\rho^2 \sin^2 \omega}{b^2} = 1 \tag{3.9}$$

where a and b are the lengths of the semimajor and semiminor axes respectively, so allowing for an inclination angle γ on the ellipse gives:

$$\rho^2 = \frac{a^2 b^2}{(\frac{a^2 + b^2}{2}) - (\frac{a^2 - b^2}{2})\cos(2\omega' - 2\gamma)}$$
(3.10)

where $\omega' = \omega + \gamma$, as illustrated in Fig. 3.4. This gives a first approximation which can then be used to iteratively float the ellipse parameters until a least-squares minimisation is reached. The resulting ellipse characterisation is illustrated in Fig. 3.5.

3.3 Error Analysis & Model Fitting

The front of the CME is determined through the multiscale decomposition and consequent rendering of a gradient magnitude space. At the third scale of the decomposition the smoothing filter is 2³ pixels wide, which we use as our error estimate in edge position. This error is input to the ellipse fitting algorithm for weighting the ellipse parameters, and a final error output is produced for each ellipse fit. In the case of a fading leading edge the reduced amount of points along the front will increase the error on our analysis accordingly. The final errors are displayed in the height-time plots of the CMEs, and are used in the velocity and acceleration calculations. The derivative is a 3-point Lagrangian interpolation, so there is an enhancement of error at the edges of the data sets.

The errors on the heights are used to constrain the best fit to a constant acceleration model of the form:

$$h(t) = h_0 + v_0 t + \frac{1}{2} a_0 t^2 \tag{3.11}$$

where t is time and a_0 , v_0 and h_0 are the acceleration, initial velocity and initial height respectively. This provides a linear fit to the derived velocity points and a constant fit to the acceleration.

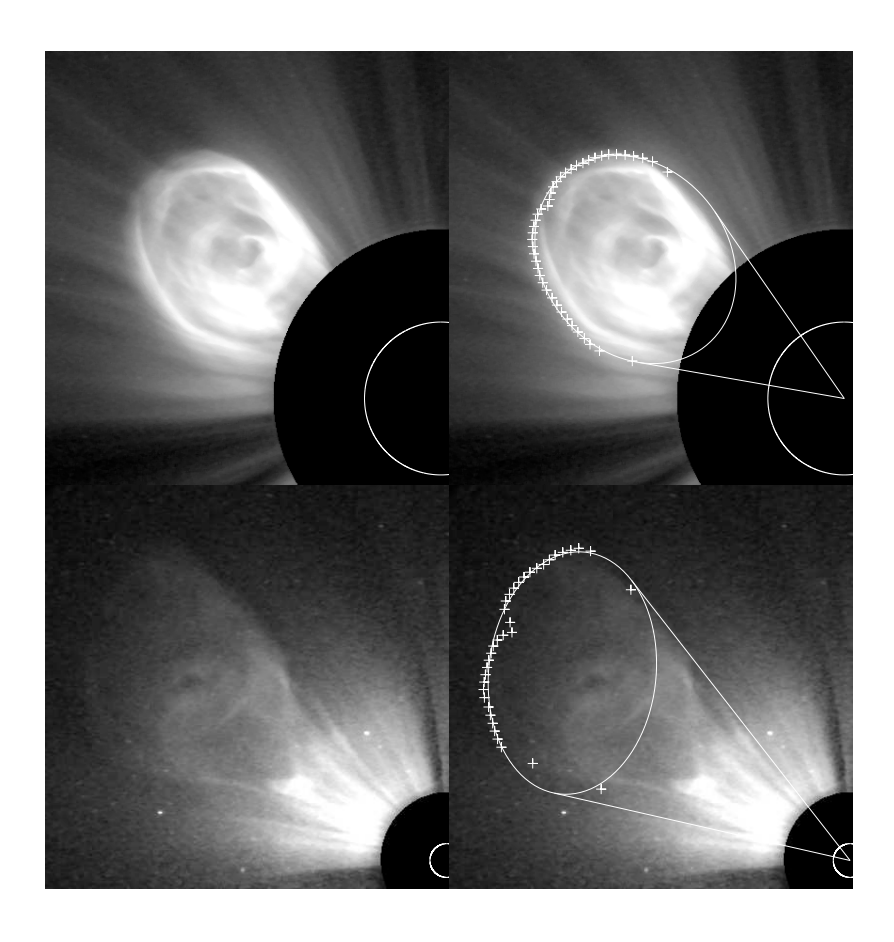


Figure 3.5: Left, the 2004 April 1 CME in C2 (top) and C3 (bottom), and right, the corresponding ellipse fit to the multiscale edge detection.

Chapter 4

Results

This section outlines some events which have been analyzed using our multiscale methods (a more detailed discussion is available in Byrne et al. [3]). We use data from the LASCO/C2 and C3, and SECCHI/COR1 and COR2 instruments, and preprocess the images as discussed in Sect. 3. The ellipse fitting algorithm applied to each event gives consistent heights of the CME front measured from Sun centre to the maximum height on the ellipse, and these lead to velocity and acceleration profiles of our events and provides the angular widths. In each instance we include the values from CACTus, CDAW and SEEDS catalogues, noting that CACTus lists a median speed for the whole CME, CDAW is wholly subjective, and the SEEDS detection applies only to the C2 field-of-view. The velocity, acceleration and angular width results of each method are highlighted in Tables 1, 2 and 3 below. It is clear that many of the CACTus, CDAW and SEEDS results lie outside the results and error ranges of our analysis.

4.1 Slow CME: 2004 April 1

This CME was first observed in the north-east from approximately 23:00 UT on 2004 April 1, is in the field-of-view for over 9 hours, and exhibits a bright loop front, cavity and twisted core (Fig. 3.5).

The height-time plot follows a similar trend to that of CDAW (overplotted in top Fig. 4.1 with a dashed line). The velocity-fit was found to be linearly increasing from 405 to 615 km s⁻¹, giving an acceleration of 5.9 ± 2.6 m s⁻². Note also that the kinematics of this event exhibit non-linear structure clearly seen in the velocity and acceleration profiles. The ellipse fit spans approximately 44° in C2, stepping down to approximately 38° in C3.

The CACTus catalog lists the CME as having an angular span of 66° , and a median velocity of 487 km s^{-1} . The CDAW catalog lists an angular span of 79° , a velocity of 460 km s^{-1} , and an acceleration of 7.1 m s^{-2} . The SEEDS catalog lists an angular span of 58° , a velocity of 319 km s^{-1} , and an acceleration of 12.9 m s^{-2} .

This event shows unexpected structure in the velocity and acceleration profiles which indicates a complex eruption not satisfactorily modeled with constant acceleration.

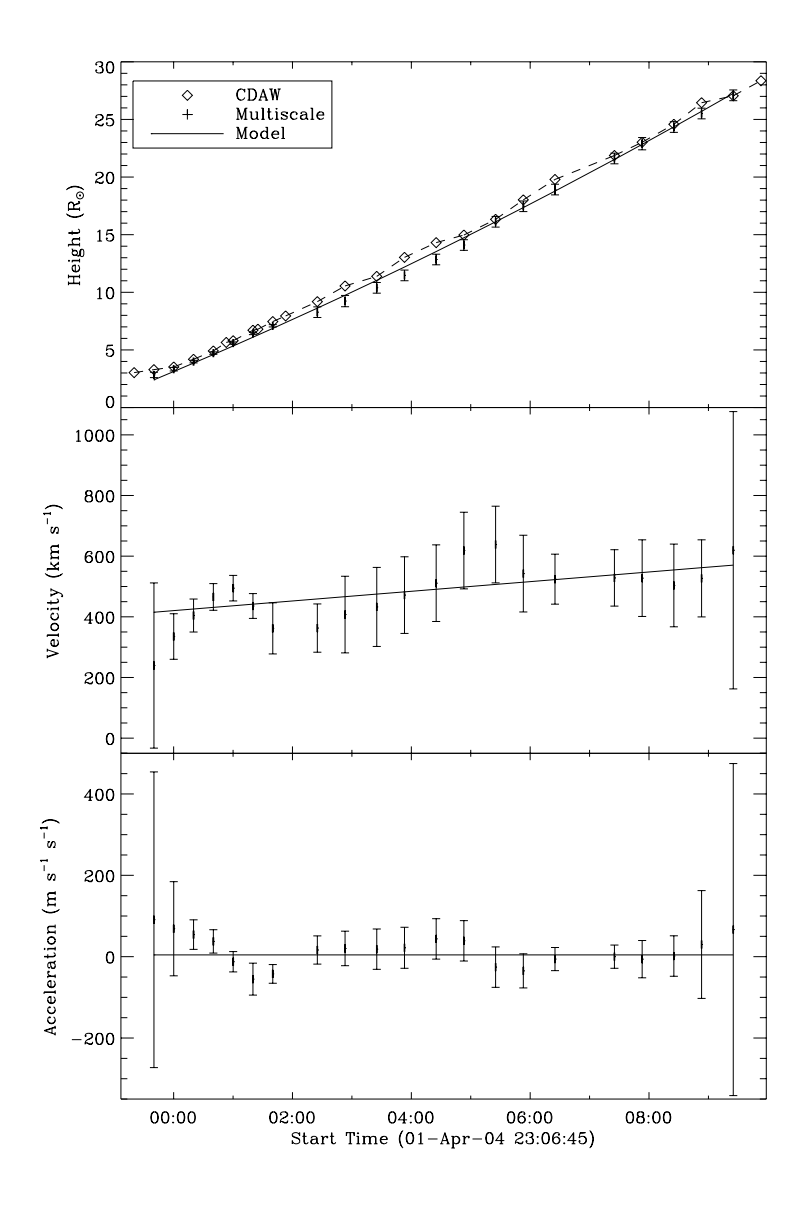


Figure 4.1: Kinematic curves for the ellipse fit to the multiscale edge detection of the 2004 April 1 CME observed by LASCO/C2 and C3. The plots from top to bottom are height, velocity and acceleration, and the CDAW heights are over-plotted with a dashed line. The fits are based upon the constant acceleration model.

4.2 Fast CME: 2002 April 21

This CME was first observed in the west from 01:27 UT on 2002 April 21. The height-time plot follows a similar trend to that of CDAW (overplotted in top Fig. 4.2 with a dashed line). The velocity-fit was found to be linearly increasing from 2 200 to 2 414 km s⁻¹, giving a constant acceleration fit of 32 ± 26 m s⁻². The ellipse fit spans 53° in C2, and shows an likely increasing trend to 65° in C3.

The CACTus catalog lists the CME as having an angular span of 352° , and a median velocity of $1\,103~\rm km~s^{-1}$. The CDAW catalog lists an angular span of 360° , a velocity of $2\,393~\rm km~s^{-1}$,

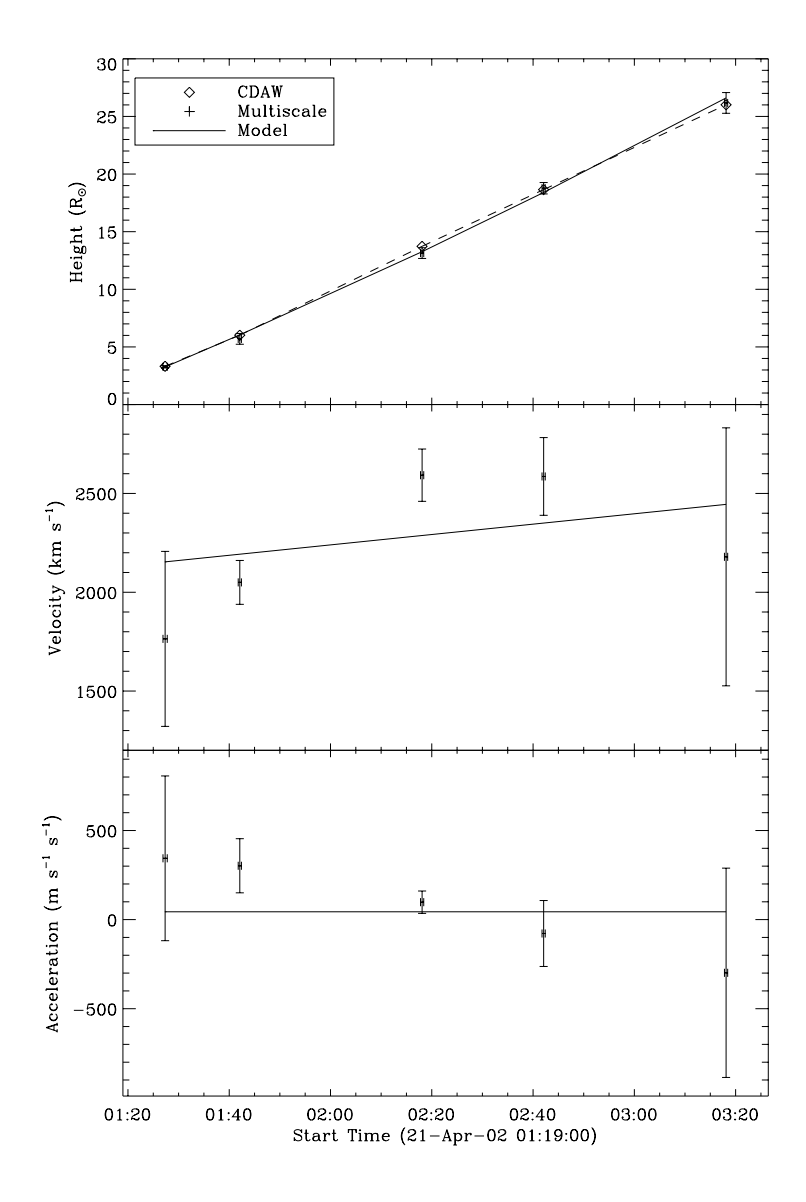


Figure 4.2: Kinematic curves for the ellipse fit to the multiscale edge detection of the 2002 April 21 CME observed by LASCO/C2 and C3. The plots from top to bottom are height, velocity and acceleration, and the CDAW heights are over-plotted with a dashed line. The fits are based upon the constant acceleration model.

and an acceleration of -1.4 m s⁻². The SEEDS catalog lists an angular span of 186° , a velocity of 702 km s⁻¹, and an acceleration of 33.5 m s⁻².

The kinematics of this event are not modeled satisfactorily by the constant acceleration model, since the fits do not lie within all error bars. The argument for a non-linear velocity profile, with a possible early decreasing acceleration, is justified for this event, although the instrument cadence limits the data set available for interpretation. The previous analysis of Gallagher et al. [9], where non-constant acceleration is implied, resulted in a velocity of $\sim\!2\,500$ km s⁻¹ past $\sim\!3.4~R_\odot$ which is consistent with our results past $\sim\!6~R_\odot$ in Fig. 4.2.

4.3. Results – Summary 20

4.3 Summary

The kinematics we produced show that the constant acceleration model may not always be appropriate. In the 2000 January 2 and 2002 April 21 events, we find good examples of the possible non-linear velocity profile and consequent non-constant acceleration profile. Indeed these events are shown to have a decreasing acceleration, possibly to zero or below, as the CMEs traverse the field-of-view. Simulations of the breakout model outlined in Lynch et al. [18] resulted in constant acceleration fits which do not agree with these observations. Other events such as 2001 April 23 and 2004 April 1 also show a possible decreasing acceleration phase early on. Furthermore, the structure seen in some events would indicate that the CME does not progress smoothly. The velocities of the 2004 April 1 CME and the 2007 November 16 CME show non-smooth profiles and may imply a form of bursty reconnection or other staggered energy release driving the CME. Other profiles may show a stepwise pattern, indicative of separate regimes of CME progression. None of the current CME models indicate a form of non-smooth progression, although the 2D flux-rope model does describe an early acceleration regime giving a non-linear velocity to the eruption (see Fig. 11.5 in [23]).

It may be concluded that the angular widths of the events are indicative of whether the CME expands radially or otherwise in the plane-of-sky. For the CMEs studied above, the observations of 2000 April 18, 2000 April 23 and 2002 April 21 show a super-radial expansion. These events also show high velocities, obtaining top speeds of up to 1 000 km s⁻¹, over 1 100 km s⁻¹ and 2 500 km s⁻¹ respectively, and may therefore indicate a link between the CME expansion and speed. Furthermore, it is suggested by Krall and St. Cyr [17] that the flux-rope model can account for different observed expansion rates due to the axial versus broadside view of the erupting flux system.

Table 4.1: Summary of CME velocities as measured by CACTus, CDAW, SEEDS and multiscale methods.

Date	CACTus	CDAW	SEEDS	Multiscale
		${\rm km}~{\rm s}^{-1}$		
2000 Jan 02	512	603	396	385 – 772
2000 Apr 18	463	668	339	357 - 1000
2000 Apr 23	1041	1187	595	1128 - 1084
2001 Apr 23	459	530	501	580 - 450
2002 Apr 21	1103	2393	702	2200 - 2414
2004 Apr 01	487	460	319	405 - 615
2007 Oct 08	n/a	206	103	71 - 330
2007 Nov 16	n/a	326	154	131 – 483

4.3. Results – Summary

Table 4.2: Summary of CME accelerations as measured by CACTus, CDAW, SEEDS and multiscale methods.

Date	CACTus	CDAW	SEEDS	Multiscale
		${\rm m}~{\rm s}^{-2}$		
2000 Jan 02	0	21.3	-5.8	17.3 ± 4.1
2000 Apr 18	0	23.1	17.5	29.1 ± 1.6
2000 Apr 23	0	-48.5	-8.9	-4.3 ± 20.6
2001 Apr 23	0	-0.7	-1.4	-5.2 ± 1.0
2002 Apr 21	0	-1.4	33.5	32.0 ± 26.0
2004 Apr 01	0	7.1	12.9	5.9 ± 2.6
2007 Oct 08	n/a	3.4	2.4	5.7 ± 0.9
2007 Nov 16	n/a	4.9	11.0	13.7 ± 1.7

Table 4.3: Summary of CME angular widths as measured by CACTus, CDAW, SEEDS and multiscale methods.

Date	CACTus	CDAW	SEEDS	Multiscale
Date	CACTUS	CDAW	SEEDS	Multiscale
		degrees		
2000 Jan 02	160	107	96	50 - 95
2000 Apr 18	106	105	108	68 - 110
2000 Apr 23	352	360	130	106 - 130
2001 Apr 23	124	91	74	55 - 60
2002 Apr 21	352	360	186	53 - 65
2004 Apr 01	66	79	58	44 - 38
2007 Oct 08	n/a	82	59	23 - 60
2007 Nov 16	n/a	78	54	40 - 55

Chapter 5

Forward Plan

5.1 Automation

The techniques detailed above are implemented manually and work is on-going to automate these methods for analysis of large data sets. This would enable a statistical study of the kinematics and morphologies of numerous CMEs in order to compare with theoretical models. Automation would also lead to the creation of a catalogue based in the Astrophysics Research Group in Trinity. This would provide real-time monitoring (much like www.solarmonitor.org to which it may be integrated) and information on CMEs including their predicted arrival times at Earth, important for space weather forecasting.

5.2 STEREO Twin Views

The combination of STEREO's Ahead and Behind spacecraft views will lead to corrections for projection effects and help determine the true CME kinematics and 3D structure. The development of a new 3D cone-model, for example, would benefit this work. One strong event seen in both the Ahead and Behind spacecraft in March 2008 has been studied as a first effort at stereoscopic triangulation. With our developed methods of multiscale analysis and ellipse characterisation outlined above, it is possible to project planes of intersection from both views to localise the eruption in 3D space, illustrated in Fig. 5.1. This is again of great benefit to the space weather community for understanding and forecasting CME trajectories.

5.3 Error Analysis

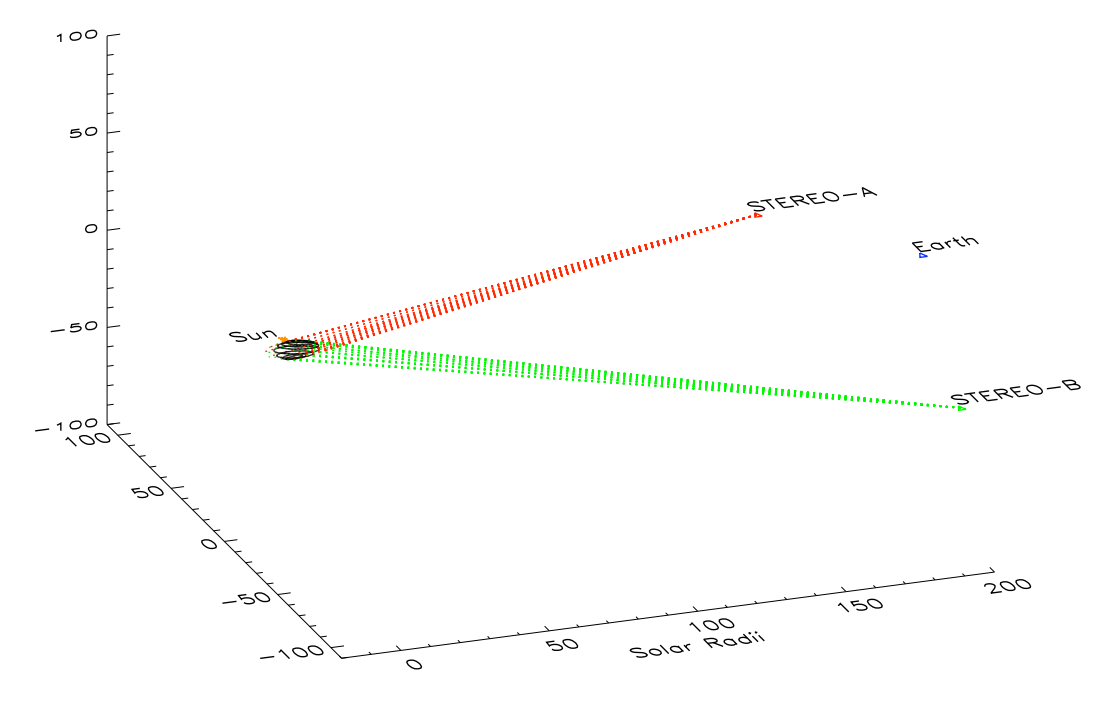
This work has produced new analysis of a sample of CME kinematics and their associated errors, through the use of multiscale tools. The possible introduction of bootstrapping to simulate the errors involved in current and future multiscale analysis may be advantageous to our work. We also intend to run a simulation to compare running-difference and multiscale methods, in order to highlight the extent to which temporal differencing can introduce errors.

5.4 Model Comparisons

Direct comparisons with the predictions of CME models will test their efficacy in describing what we observe. Since we are using and developing more accurate methods than previously available, we will be in a prime position to do this.

5.5 Multiscale tool development

The research of multiscale tools is ongoing, with a view to developing higher accuracy processing methods through the introduction of ridgelets or curvelets. Initial efforts show these may be better suited to studying the curved fronts of CMEs and enhancing their signal-to-noise ratio.



(a) Spacecraft positions relative to Earth in March 2008

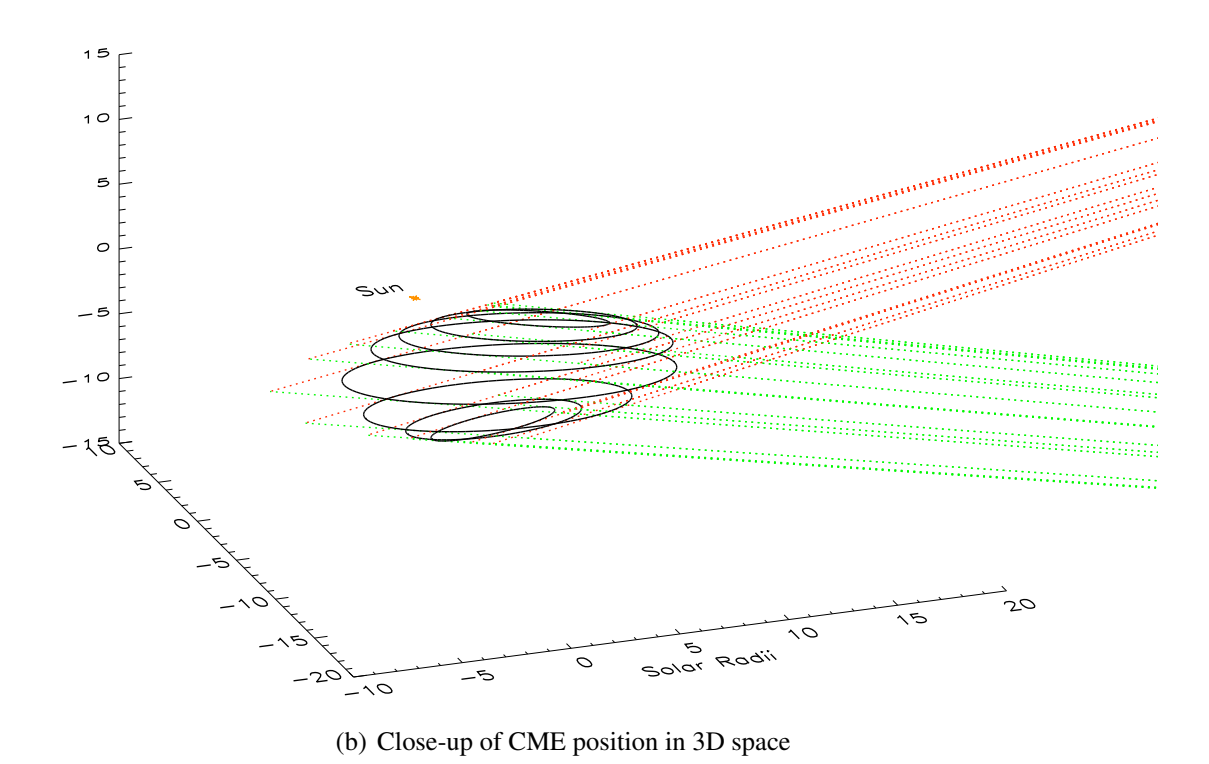


Figure 5.1: The triangulation of the planes of intersection from both spacecraft views, with ellipses fitted within the corresponding quadrilaterals, thus localising the CME front in 3D space. The red lines show the views from Ahead, the green lines show the views from Behind, and the yellow point marks Sun centre at (0,0,0). The axes are in units of solar radii in the x, y, and z planes of the ecliptic.

Chapter 6

List of Publications & Presentations

Refereed Papers:

Byrne, **J. P.**, Gallagher, P. T., McAteer, R. T. J., Young, C. A. *The Kinematics of Coronal Mass Ejections using Multiscale Methods*. Astronomy & Astrophysics (*in review*).

Conference Proceedings:

Byrne, J. P., Young, C. A., Gallagher, P. T., McAteer, R. T. J. "Multiscale Image Processing Methods" *Astronomical Society of the Pacific*, "First Results from Hinode", Vol. 397, 2007.

Conference Talks:

Byrne, J. P., Gallagher, P. T., McAteer, R. T. J., Young, C. A. "The Kinematics of CMEs using Multiscale Methods of Analysis and Characterisation" *STEREO Science Working Group*. *Observatoire de Paris-Meudon, France. March* 2008

Byrne, J. P., Gallagher, P. T., McAteer, R. T. J., Young, C. A. "Multiscale Detection and Characterisation of CMEs", *SECCHI Consortium Meeting*.

Caltech, Pasadena, USA. November 2007.

Conference Posters:

Byrne, J. P., Gallagher, P. T., McAteer, R. T. J., Young, C. A. "Multiscale Analysis of CMEs", *Solar Image Processing Workshop IV.*

Baltimore, MD, USA. October 2008

Byrne, J. P., Gallagher, P. T., McAteer, R. T. J., Young, C. A. "The Kinematics of CMEs using Multiscale Methods", *RAS National Astronomy Meeting*,

Queen's University Belfast, Northern Ireland. April 2008

Byrne, J. P., Gallagher, P. T., McAteer, R. T. J., Young, C. A. "The Kinematics of CMEs using Multiscale Methods" 1st SMESE Workshop,

Institut dAstrophysique de Paris, France. March 2008.

Byrne, J. P., Gallagher, P. T., McAteer, R. T. J., Young, C. A. "Automated Detection & Characterisation of CMEs" *RAS National Astronomy Meeting*,

UCLan, Preston, Lancashire, England. April 2007.

Young, C. A., Ireland, J., McAteer, R. T. J., Gallagher P. T., **Byrne, J. P.** "Multiscale Tools for Solar Image Processing" *American Geophysical Union, Fall Meeting, San Francisco, CA, USA. December 2007.*

Young, C. A., **Byrne, J. P.**, Ireland, J., Gallagher P. T., McAteer, R. T. J. "Multiscale Solar Image Processing" *American Geophysical Union, Fall Meeting, San Francisco, CA, USA. December 2006.*

Acknowledgements

This work is supported by a grant from Science Foundation Ireland's Research Frontiers Programme.

Bibliography

- [1] S. K. Antiochos, C. R. DeVore, and J. A. Klimchuk. A Model for Solar Coronal Mass Ejections. *Astrophysical Journal*, 510:485–493, 1999. URL http://adsabs.harvard.edu/abs/1999ApJ...510..485A.
- [2] G. E. Brueckner, R. A. Howard, M. J. Koomen, C. M. Korendyke, D. J. Michels, J. D. Moses, D. G. Socker, K. P. Dere, P. L. Lamy, A. Llebaria, M. V. Bout, R. Schwenn, G. M. Simnett, D. K. Bedford, and C. J. Eyles. The Large Angle Spectroscopic Coronagraph (LASCO). *Solar Physics*, 162:357–402, 1995. URL http://adsabs.harvard.edu/abs/1995SoPh..162..357B.
- [3] J. P. Byrne, P. T. Gallagher, R. T. J. McAteer, and C. A. Young. The Kinematics of CMEs using Multiscale Methods. *Astronomy & Astrophysics (in review)*, 2008.
- [4] P. J. Cargill. On the Aerodynamic Drag Force Acting on Interplanetary Coronal Mass Ejections. *Solar Physics*, 221:135–149, 2004. URL http://adsabs.harvard.edu/abs/2004SoPh..221..135C.
- [5] J. Chen, R. A. Howard, G. E. Brueckner, R. Santoro, J. Krall, S. E. Paswaters, O. C. St. Cyr, R. Schwenn, P. Lamy, and G. M. Simnett. Evidence of an Erupting Magnetic Flux Rope: LASCO Coronal Mass Ejection of 1997 April 13. *Astrophysical Journal*, 490: L191, 1997. URL http://adsabs.harvard.edu/abs/1997ApJ...490L.191C.
- [6] J. Chen and J. Krall. Acceleration of coronal mass ejections. *Journal of Geophysical Research (Space Physics)*, 108:1410, 2003.
- [7] M. Fligge and S. K. Solanki. Noise reduction in astronomical spectra using wavelet packets. *Astronomy & Astrophysics Supplement Series*, 124:579–587, 1997. URL http://adsabs.harvard.edu/abs/1997A 26AS..124..579F.
- [8] T. G. Forbes and E. R. Priest. Photospheric Magnetic Field Evolution and Eruptive Flares. Astrophysical Journal, 446:377, 1995. URL http://adsabs.harvard.edu/abs/1995ApJ...446..377F.
- [9] P. T. Gallagher, G. R. Lawrence, and B. R. Dennis. Rapid Acceleration of a Coronal Mass Ejection in the Low Corona and Implications for Propagation. *Astrophysical Journal*, 588: L53–L56, 2003. URL http://adsabs.harvard.edu/abs/2003ApJ...588L..53G.

BIBLIOGRAPHY 28

[10] N. Gopalswamy, S. Yashiro, M. L. Kaiser, R. A. Howard, and J.-L. Bougeret. Characteristics of coronal mass ejections associated with long-wavelength type II radio bursts. *Journal of Geophysics Research*, 106:29219–29230, 2001. URL http://adsabs.harvard.edu/abs/2001JGR...10629219G.

- [11] J. T. Gosling, E. Hildner, R. M. MacQueen, R. H. Munro, A. I. Poland, and C. L. Ross. The speeds of coronal mass ejection events. *Solar Physics*, 48:389–397, 1976. URL http://adsabs.harvard.edu/abs/1976SoPh...48..389G.
- [12] R. J. Hewett, P. T. Gallagher, R. T. J. McAteer, C. A. Young, J. Ireland, P. A. Conlon, and K. Maguire. Multiscale Analysis of Active Region Evolution. *Solar Physics*, 248: 311–322, 2008. URL http://adsabs.harvard.edu/abs/2008SoPh..248..311H.
- [13] R. A. Howard, J. D. Moses, and D. G. Socker. Sun-Earth connection coronal and heliospheric investigation (SECCHI). *Proceedings of the SPIE*, 4139:259–283, 2000. URL http://adsabs.harvard.edu/abs/2000SPIE.4139..259H.
- [14] A. J. Hundhausen, A. L. Stanger, and S. A. Serbicki. Mass and energy contents of coronal mass ejections: SMM results from 1980 and 1984-1988. *Proc. 3rd SOHO Workshop*, SP-373:409–412, 1994. URL http://adsabs.harvard.edu/abs/1994ESASP.373..409H.
- [15] P. A. Isenberg, T. G. Forbes, and P. Demoulin. Catastrophic Evolution of a Force-free Flux Rope: A Model for Eruptive Flares. *Astrophysical Journal*, 417:368–+, November 1993.
- [16] J. Krall, J. Chen, R. T. Duffin, R. A. Howard, and B. J. Thompson. Erupting Solar Magnetic Flux Ropes: Theory and Observation. *Astrophysical Journal*, 562:1045–1057, 2001. URL http://adsabs.harvard.edu/abs/2001ApJ...562.1045K.
- [17] J. Krall and O. C. St. Cyr. Flux-Rope Coronal Mass Ejection Geometry and Its Relation to Observed Morphology. *Astrophysical Journal*, 652:1740–1746, 2006. URL http://adsabs.harvard.edu/abs/2006ApJ...652.1740K.
- [18] B. J. Lynch, S. K. Antiochos, P. J. MacNeice, T. H. Zurbuchen, and L. A. Fisk. Observable Properties of the Breakout Model for Coronal Mass Ejections. *Astrophysical Journal*, 617: 589–599, 2004. URL http://adsabs.harvard.edu/abs/2004ApJ...617..589L.
- [19] P. MacNeice, S. K. Antiochos, P. Phillips, D. S. Spicer, C. R. DeVore, and K. Olson. A Numerical Study of the Breakout Model for Coronal Mass Ejection Initiation. *Astrophysical Journal*, 614:1028–1041, 2004. URL http://adsabs.harvard.edu/abs/2004ApJ...614.1028M.
- [20] Y.-J. Moon, J. Chae, G. S. Choe, H. Wang, Y. D. Park, and C. Z. Cheng. Low Atmosphere Reconnections Associated with an Eruptive Solar Flare. *J. Korean Astro. Soc.*, 37:41–53, 2004. URL http://adsabs.harvard.edu/abs/2004JKAS...37...41M.

BIBLIOGRAPHY 29

[21] F. Murtagh, J.-L. Starck, and A. Bijaoui. Image restoration with noise suppression using a multiresolution support. *Astronomy & Astrophysics Supplement Series*, 112:179–189, 1995. URL http://adsabs.harvard.edu/abs/1995A 26AS..112..179M.

- [22] O. Olmedo, J. Zhang, H. Wechsler, A. Poland, and K. Borne. Automatic Detection and Tracking of Coronal Mass Ejections in Coronagraph Time Series. *Solar Physics*, 248: 485–499, 2008. URL http://adsabs.harvard.edu/abs/2008SoPh..248..4850.
- [23] E. Priest and T. Forbes. *Magnetic Reconnection*. Cambridge University Press, UK, jun 2000.
- [24] E. R. Priest and T. G. Forbes. Magnetic field evolution during prominence eruptions and two-ribbon flares. *Solar Physics*, 126:319–350, April 1990.
- [25] E. Robbrecht and D. Berghmans. Automated recognition of coronal mass ejections (CMEs) in near-real-time data. *Astronomy & Astrophysics*, 425:1097–1106, 2004. URL http://adsabs.harvard.edu/abs/2004A 26A...425.1097R.
- [26] G. Stenborg and P. J. Cobelli. A wavelet packets equalization technique to reveal the multiple spatial-scale nature of coronal structures. *Astronomy & Astrophysics*, 398:1185–1193, 2003. URL http://adsabs.harvard.edu/abs/2003A 26A...398.1185S.
- [27] G. Stenborg, A. Vourlidas, and R. A. Howard. Fresh View Α Extreme-Ultraviolet Corona from the Application of a New Image-Astrophysical Journal, 674:1201–1206, Processing Technique. URL http://adsabs.harvard.edu/abs/2008ApJ...674.1201S.
- [28] S. Yashiro, N. Gopalswamy, G. Michalek, O. C. St. Cyr, S. P. Plunkett, N. B. Rich, and R. A. Howard. A catalog of white light coronal mass ejections observed by the SOHO spacecraft Measurements. *Journal of Geophysics Research*, 109:A7, 2004.
- [29] C. P. Gallagher. A. Young and T. Multiscale Edge Detecthe Corona. Solar Physics, 248:457-469, 2008. **URL** http://adsabs.harvard.edu/abs/2008SoPh..248..457Y.
- [30] J. Zhang and J. Wang. Are Homologous Flare-Coronal Mass Ejection Events Triggered by Moving Magnetic Features? Astrophysical Journal, 566:L117–L120, 2002. URL http://adsabs.harvard.edu/abs/2002ApJ...566L.117Z.